



Rethinking Boundary Detection in Deep Learning-Based Medical Image Segmentation

Yi Lin^{a,1}, Dong Zhang^{b,1}, Xiao Fang^{a,1}, Yufan Chen^c, Kwang-Ting Cheng^{a,b}, Hao Chen^{a,c,d,*}

^aDepartment of Computer Science and Engineering, The Hong Kong University of Science and Technology, Hong Kong, China

^bDepartment of Electronic and Computer Engineering, The Hong Kong University of Science and Technology, Hong Kong, China.

^cDepartment of Chemical and Biological Engineering, The Hong Kong University of Science and Technology, Hong Kong, China

^dHKUST Shenzhen-Hong Kong Collaborative Innovation Research Institute, Futian, Shenzhen, China.

ARTICLE INFO

Article history:

Keywords:

Medical image segmentation,
Convolutional neural networks,
Vision Transformer,
Network architecture,
Boundary detection.

ABSTRACT

Medical image segmentation is a pivotal task within the realms of medical image analysis and computer vision. While current methods have shown promise in accurately segmenting major regions of interest, the precise segmentation of boundary areas remains challenging. In this study, we propose a novel network architecture named CTO, which combines Convolutional Neural Networks (CNNs), Vision Transformer (ViT) models, and explicit edge detection operators to tackle this challenge. CTO surpasses existing methods in terms of segmentation accuracy and strikes a better balance between accuracy and efficiency, without the need for additional data inputs or label injections. Specifically, CTO adheres to the canonical encoder-decoder network paradigm, with a dual-stream encoder network comprising a mainstream CNN stream for capturing local features and an auxiliary StitchViT stream for integrating long-range dependencies. Furthermore, to enhance the model's ability to learn boundary areas, we introduce a boundary-guided decoder network that employs binary boundary masks generated by dedicated edge detection operators to provide explicit guidance during the decoding process. We validate the performance of CTO through extensive experiments conducted on seven challenging medical image segmentation datasets, namely ISIC 2016, PH2, ISIC 2018, CoNIC, LiTS17, and BTCV. Our experimental results unequivocally demonstrate that CTO achieves state-of-the-art accuracy on these datasets while maintaining competitive model complexity. The codes have been released at: CTO.

© 2025 Elsevier B. V. All rights reserved.

1. Introduction

Medical image segmentation (MedISeg) is a fundamental yet challenging task that poses several significant research topics in both the medical image analysis and computer vision domains (Zhang et al., 2022a; Lin et al., 2023b; Xiao et al., 2023). The primary objective of MedISeg is to accurately identify and localize semantic lesions or anatomical structures within medical images obtained through imaging modalities such as

Computed Tomography, X-ray, and Magnetic Resonance Imaging (Ronneberger et al., 2015; Lin et al., 2021; Zhang et al., 2022a). In recent years, MedISeg has garnered extensive attention and has been extensively investigated due to its potential applications in fields such as robotic surgery (Gao et al., 2021), cancer diagnosis (Lin et al., 2019, 2024), and treatment planning (Wijeratne et al., 2021). To achieve satisfactory segmentation results in clinical practice, it is imperative to extract a comprehensive yet discriminative set of semantic feature representations (Zhang et al., 2022a; Lin et al., 2025). In the field of image processing, the vision transformer (ViT) architecture has emerged as a potential tool for enhancing accuracy

*Corresponding author: Hao Chen (E-mail: jhc@cse.ust.hk).

¹These three authors contributed equally to this work.

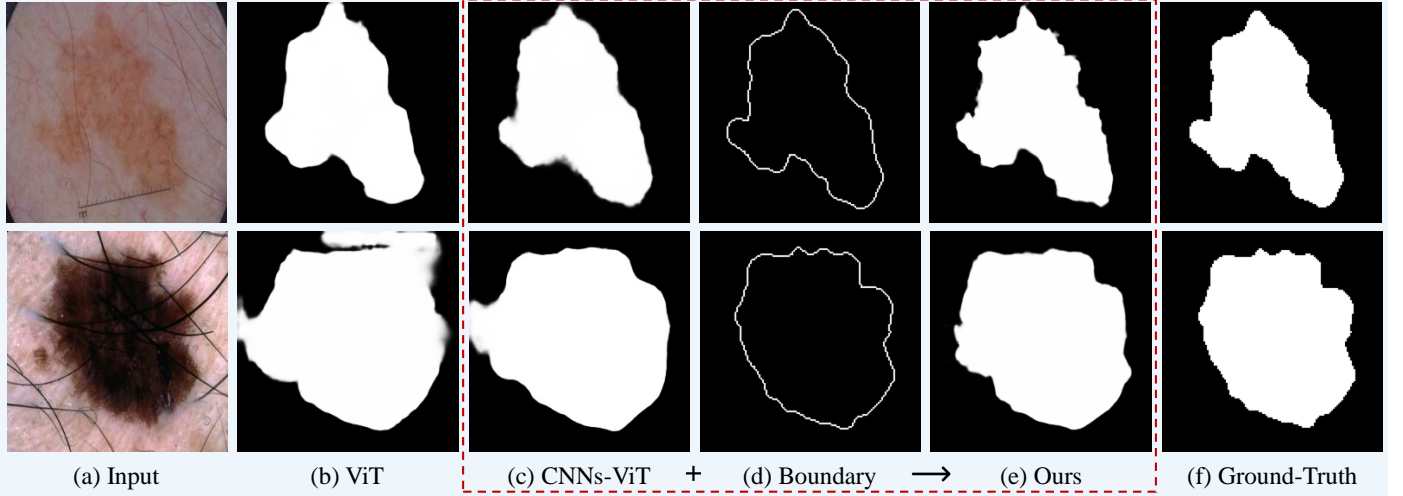


Fig. 1. Visualization comparisons of medical image segmentation results obtained from ViT (Dosovitskiy et al., 2020), CNNs-ViT (Hatamizadeh et al., 2022a), boundary detection operator (Kanopoulos et al., 1988), and our proposed CTO. The results demonstrate that our method, which incorporates the explicit boundary detection operator in MedISeg, can achieve a significant improvement, especially in boundary areas, indicating the importance and effectiveness of the boundary detection operator in MedISeg. The red dashed bounding box highlights the core idea of our method. Samples are from the ISIC dataset (Gutman et al., 2016; Codella et al., 2019).

in medical image recognition tasks when compared to methods based on convolutional neural networks (CNNs) (Hatamizadeh et al., 2022b; Zhang et al., 2022b). ViT-based approaches have achieved state-of-the-art performance in various fundamental medical image analysis tasks, such as image diagnosis (Wu et al., 2022), semantic segmentation (Chen et al., 2024), and object detection (Shamshad et al., 2023), primarily due to their ability to capture long-range feature dependencies. As illustrated in Figure 1(b), a ViT-based model effectively encompasses all the relevant pixels within the target area (Dosovitskiy et al., 2020). A typical ViT-based MedISeg framework involves partitioning the input medical image into several image patches, which serve as image tokens for interactions through multi-head self-attention layers (Vaswani et al., 2017). Subsequently, a positional embedding layer may be employed to capture relative position information, if deemed necessary (Zhang et al., 2023). Layer normalization strategies and feature regularization operations are then applied to generate the output predictions. These operations, along with specific layers, are interconnected to form a foundational transformer block, which is recurrently employed to encode valuable semantic representations for the task-specific head network.

Despite the success in capturing long-range feature dependencies, current ViT approaches exhibit limitations in terms of translation invariance and local feature representation (Chen et al., 2024; Yuan et al., 2023), which are crucial for MedISeg (Zhang et al., 2022a; Shamshad et al., 2023; Yan et al., 2022; Xiao et al., 2023). To address these limitations, progressive methods, such as CNNs-ViT hybrid architectures, have been proposed for MedISeg, including TransUNet (Chen et al., 2024), UNETR (Hatamizadeh et al., 2022b), and Swin UNETR (Hatamizadeh et al., 2022a). These methods typically employ a specific network architecture as the primary framework and augment their learning capabilities by incorporating auxiliary learning modules (Xiao et al., 2023; Shamshad et al.,

2023). For example, convolution layers are introduced to a ViT framework to capture local features, or Transformer layers are integrated into a CNNs framework to capture global features, enabling the ViT/CNNs model to acquire more informative yet elusive local/global features. Particularly, CNNs-ViT hybrid approaches for MedISeg are commonly based on the UNet framework (Ronneberger et al., 2015), with multi-scale learning blocks and skip connections (Huang et al., 2021) incorporated into the backbone network (Hatamizadeh et al., 2022b). As depicted in Figure 1(c), the CNNs-ViT hybrid method achieves superior predictions in the local region of the foreground object when compared to the results in (b).

Boundary information matters in MedISeg (Lin et al., 2023b; Wang et al., 2022; Lee et al., 2020). Regrettably, current deep learning models often neglect this critical aspect in vision recognition tasks (Wang et al., 2022; Lee et al., 2020; Zhang et al., 2020a). Explicitly incorporating boundary learning patterns, as opposed to implicit feature learning models, can offer significant advantages in terms of straightforward implementation, high efficiency, and purposeful objectives (Fan et al., 2020; Wang et al., 2022; Bokhovkin and Burnaev, 2019; Wang et al., 2021; Hatamizadeh et al., 2019). Recently, edge detection operators have been successfully deployed in pixel-level recognition and generation tasks to explicitly enhance the learning capacity for localization (Chen et al., 2021; Fan et al., 2020; Lin et al., 2023a). In the context of MedISeg tasks, we firmly believe that the edge detection operator should assume a prominent role, as it can provide explicit priors for segmentation tasks. As depicted in Figure 1(d), the boundary of the foreground object-of-interest can be accurately extracted using the edge detection operator (Kanopoulos et al., 1988). Moreover, the adoption of an explicit learning strategy can empirically enhance the feature representation capacity of the segmentation model.

In this paper, we introduce a novel network architecture, named CTO (*i.e.*, Convolution, Transformer, and Operator), for

MedISeg that seamlessly integrates CNNs, ViT, and edge detection operators to effectively harness local features, long-range feature dependencies, and explicit object boundaries. CTO follows the conventional encoder-decoder paradigm, wherein the encoder network comprises a CNNs network stream and a StitchViT network stream. The fusion of the feature maps obtained from these two streams serves as the input for the decoder network. To bolster the capacity for boundary learning, we introduce a boundary-guided decoder network that utilizes a self-generated boundary mask, extracted through edge detection operators, as explicit supervisory signals to guide the decoding learning process. The proposed CTO can achieve higher segmentation accuracy and a better trade-off between accuracy and efficiency compared to current MedISeg methods. More importantly, CTO does not require any additional data inputs or label injections. As depicted in Figure 1 (e), our method outperforms advanced CNNs-ViT hybrid architectures by effectively capturing all pixel areas of the object and generating precise predictions at the boundary regions. We thoroughly evaluate the performance of CTO on seven representative yet challenging MedISeg datasets, including ISIC 2016, ISIC 2018 (Gutman et al., 2016; Codella et al., 2019), PH2 (Mendonça et al., 2013), CoNIC (Graham et al., 2021b), LiTS17 (Bilic et al., 2023), MSD BraTS (Antonelli et al., 2022), and BTCV (Irshad et al., 2023). Our extensive experimental results demonstrate that CTO achieves the following: 1) higher accuracy on these datasets; 2) a considerable performance margin over state-of-the-art methods; 3) competitive model complexity and efficiency.

The main contributions of this paper are threefold:

- We investigate their fundamental components (*i.e.*, CNN, Transformer, and Operator) by proposing a network architecture, CTO, that investigate the effectiveness of boundary detection in medical image segmentation from the perspective of feature extraction and information fusion.
- We propose a novel StitchViT network that captures both global and local feature dependencies while maintaining a low computational cost.
- We propose a boundary-guided decoder network that uses a self-generated boundary mask as supervisions to enhance boundary learning capacity.
- Our proposed CTO achieves state-of-the-art accuracy on seven MedISeg benchmarks. Extensive ablation studies demonstrate its effectiveness and efficiency.

This paper significantly extends our previous work published at IPMI 2023 (Lin et al., 2023b). Specifically, (a) we enhance the network architecture of the ViT stream by proposing StitchViT network, which captures the global feature dependencies while maintaining the local information in a low computational cost; (b) we provide a theoretical analysis to illustrate the rationale and effectiveness of our proposed method, and highlight its advantages in medical image segmentation; (c) we perform additional ablation studies, present more comprehensive experimental results, and provide more insightful result analyses.

2. Related Work

2.1. Medical Image Segmentation (MedISeg)

Thanks to the rapid development of advanced image processing methods based on deep learning technology, MedISeg technology has also made significant progress and has been extensively studied (Dosovitskiy et al., 2020; Xiao et al., 2023; Yu and Helwig, 2022). MedISeg has also been applied in practical clinical applications. Existing methods can be broadly categorized into the following three categories: i) CNN-based methods, ii) ViT-based methods, and iii) CNN-ViT hybrid methods. In category i, representative methods include VNet (Milletari et al., 2016), UNet (Ronneberger et al., 2015), Attention UNet (Schlemper et al., 2019), which uses CNNs as the backbone to extract fundamental image features and incorporate semantic segmentation tricks such as skip connections (Zhang et al., 2021a), multi-scale representation (Chen et al., 2016), and feature interaction to enhance feature representations (Chen et al., 2018). However, these methods may result in incomplete segmentation masks due to the inherently local nature of convolutions. In category ii, Swin-UNet (Cao et al., 2021) and MissFormer (Huang et al., 2021) utilize ViT to aggregate long-range feature dependencies, replacing CNNs as the encoder/decoder. However, due to the limited number of annotated medical images and small inherent variability, these methods are difficult to optimize and have high computational costs. In category iii, such as TransUNet (Chen et al., 2024), UNETR (Hatamizadeh et al., 2022b), UNETR++ (Shaker et al., 2024) and Swin-UNETR (Hatamizadeh et al., 2022a), methods combine the advantages of both CNNs and ViT, capturing both local information and long-range feature dependencies (Zhao et al., 2024). However, these methods are computationally intensive and suffer from high computational overheads. In this work, we propose a novel approach to leverage the benefits of both CNNs and ViT in the encoder process for improved MedISeg performance. We introduce StitchViT as a supplementary stream, which combines the advantages of both CNNs and ViT frameworks. Moreover, we incorporate an explicit edge detection operator to generate a self-generated boundary mask that guides the decoding learning process.

2.2. Operators in Image Processing

In digital image processing domain, operators are mathematical functions that are used to extract relevant information, enhance images, or segment regions of interest (Burger and Burge, 2022). In general, edge detection operators in image processing tasks are a type of operator that detect edges or boundaries in digital images, which are important features in many computer vision tasks, including image segmentation. In image processing tasks, operators can mainly be divided into two categories: first-order derivative operators and second-order derivative operators. For the first-order derivative operators, there are Roberts, Prewitt, and Sobel (Wang, 2007; Kamgar-Parsi and Rosenfeld, 1999). For the second-order derivative operators, there is Laplacian (Kanopoulos et al., 1988). These operators are commonly used for image edge detection tasks. Recently,

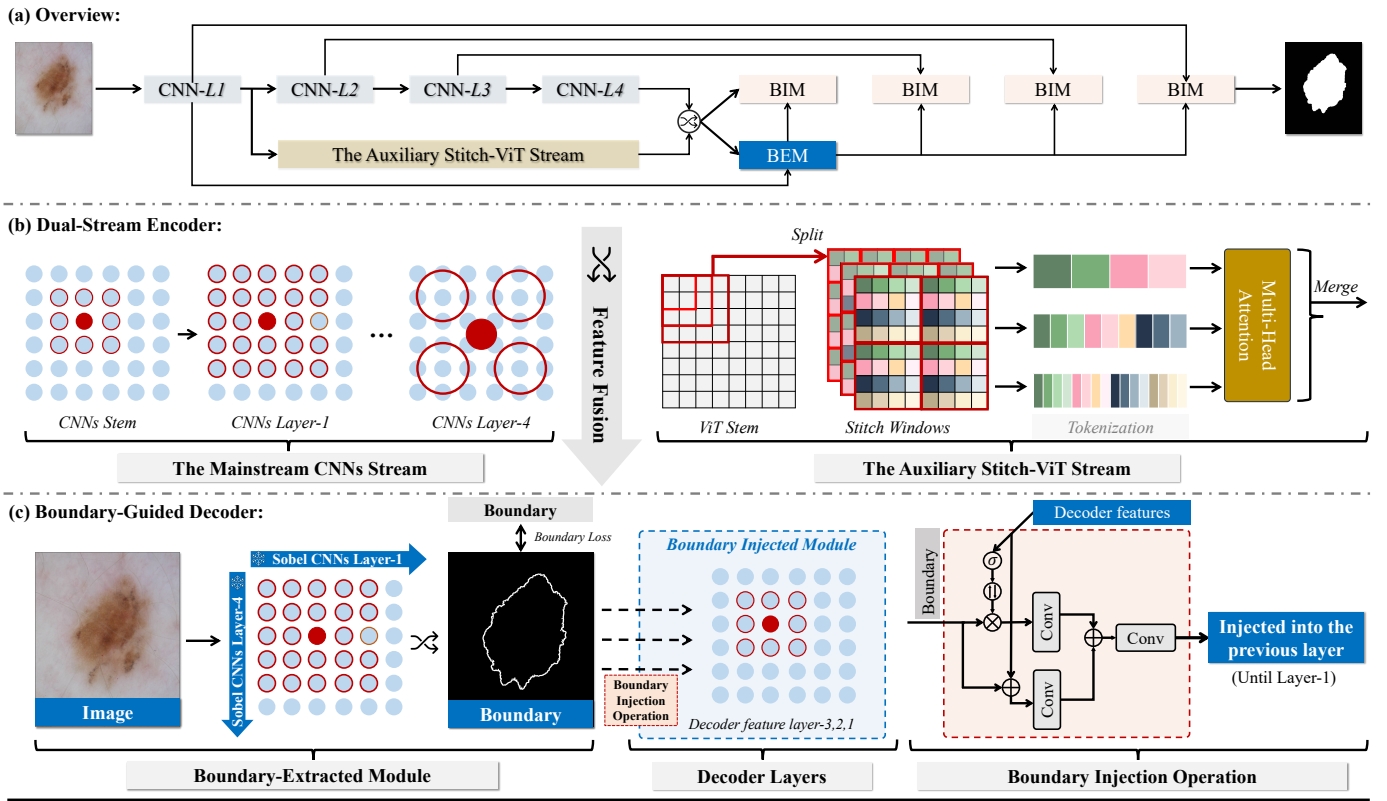


Fig. 2. (a) Illustration of our proposed Convolution, Transformer, and Operator (CTO), which follows an encoder-decoder paradigm. The dual-stream encoder network consists of a mainstream CNNs stream in the left side of (b) and an auxiliary ViT stream in the right side of (b), and the outputs of these two streams are fused together and used as the input of the decoder network. The boundary-guided decoder network in (c) employs an explicit boundary-enhanced module to guide its learning process. Specifically, the boundary detection operator is utilized to generate a self-generated boundary mask via the boundary-enhanced module that is then incorporated into the decoder network to enhance the boundary learning capacity and improve the segmentation accuracy. CTO integrates CNNs, ViT, and boundary detection into a unified framework. The red circle denotes the effective receptive field of the CNNs model, while the colored boxes represent the sliding windows of the ViT model.

edge detection operators have been applied to pixel-level computer vision tasks, such as manipulation detection and camouflaged object detection, where the goal is to detect subtle differences or manipulations in the image at a pixel-level (Chen et al., 2021; Kanopoulos et al., 1988; Shi et al., 2023). In this work, we propose to use the Sobel operator as an explicit mask extractor to guide an implicit feature learning model for MedISeg. We utilize feature maps of the intermediate layer to synthesize a high-quality binary boundary prediction mask without requiring any additional data or annotations.

3. Methodology

3.1. Overview

The overall network architecture of the proposed CTO is illustrated in Figure 2(a), which consists of a dual-stream encoder network in Figure 2(b) and a boundary-guided decoder network in Figure 2(c). For an input medical image $X \in \mathbb{R}^{H \times W \times 3}$ with a spatial resolution of $H \times W$ and three channels, we aim to predict a pixel-wise label map (*i.e.*, the semantic segmentation mask) Y , where each pixel has been assigned a predefined class label. The whole network is trained in an end-to-end manner following an encoder-decoder paradigm, which adopts skip connections to aggregate low-level features from

the encoder network to the decoder network. Specifically, for the encoder network, we propose a dual-stream encoder (*ref.* Sec. 3.2), which concurrently combines a mainstream CNNs network (*i.e.*, Res2Net (Gao et al., 2019)) and an auxiliary lightweight vision transformer network with ‘Stitch’ operation (*i.e.*, StitchViT) to capture short-range feature dependencies and long-range feature dependencies, respectively. Such a combined architecture can address the problems of incomplete foreground (due to the lack of local features) and incomplete background (due to the lack of global features) of segmentation masks as much as possible. Particularly, thanks to the efficient sliding-window operation in StitchViT, such the combination will not bring many computational overheads. After fusing feature maps of CNNs and ViT streams via feature concatenation along the channel dimension, the resulting fused output is then utilized as input to decoder network. In the boundary-guided decoder network (*ref.* Sec. 3.3), an boundary-extracted module (BEM) is first employed, which utilizes a classical Sobel (Kanopoulos et al., 1988) edge detection operator to extract a binary boundary mask from the first and fourth layer features of the CNNs. Then, this self-generated boundary mask is incorporated into every intermediate layer of the decoder network via the boundary-injected module (BIM) to guide its learning process, enabling the entire network to learn accurate object

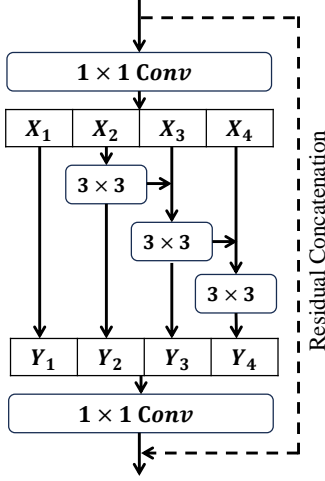


Fig. 3. Basic module of Res2Net Gao et al. (2019).

boundaries through deep supervision patterns (Li et al., 2018).

3.2. Dual-Stream Encoder Network

3.2.1. The CNNs Stream

The CNNs stream is utilized to capture short-range feature dependencies (*i.e.*, local context features) of the input image. To accomplish this, we choose Res2Net (Gao et al., 2019), an efficient and powerful CNNs backbone that comprises one convolutional stem and four Res2Net blocks. Each Res2Net block consists of several basic Res2Net modules, where each module has a scale dimension of 4. As illustrated in Figure 3, the basic Res2Net module is a variant of the classical ResNet module (He et al., 2016) that employs the split attention mechanism to capture multi-scale feature representations, *i.e.*, X_1 to X_4 . These multi-scale features obtained in each module are first concatenated together in a cascaded manner via 3×3 convolutional operation (*i.e.*, Y_1 to Y_4) and then concatenated along the channel dimension using a 1×1 convolutional operation to form the output of the basic Res2Net module. Based on Res2Net, the CNNs backbone network can generate feature maps F_c with a spatial resolution of $H/4 \times W/4$, $H/8 \times W/8$, $H/16 \times W/16$, and $H/32 \times W/32$, respectively. $c = 1, 2, \dots, 4$ denotes the index of the layer where the output feature is located. Unless stated otherwise, we follow the default architecture and settings of the Res2Net backbone as described in the referenced paper.

3.2.2. The Auxiliary ViT Stream

In addition to short-range feature dependencies, long-range feature dependencies also matter for MediSeg (Chen et al., 2024; Zhang et al., 2022a; Yuan et al., 2023; Hatamizadeh et al., 2024). To address this, we introduce the StitchViT, a vision transformer within the CTO framework. The StitchViT effectively captures long-range feature dependencies across different feature scales through the stitch operation. Figure 4 illustrates the implementation process of a StitchViT block on the input feature map $F_c \in \mathbb{R}^{\frac{H}{4} \times \frac{W}{4} \times C}$, where C is the number of channel. Initially, the input feature map is divided into multiple patches using the stitch operation. We define a dilation rate $s \in \mathbb{N}^+$ to control the degree of sparsity. In this study, we set the stitch

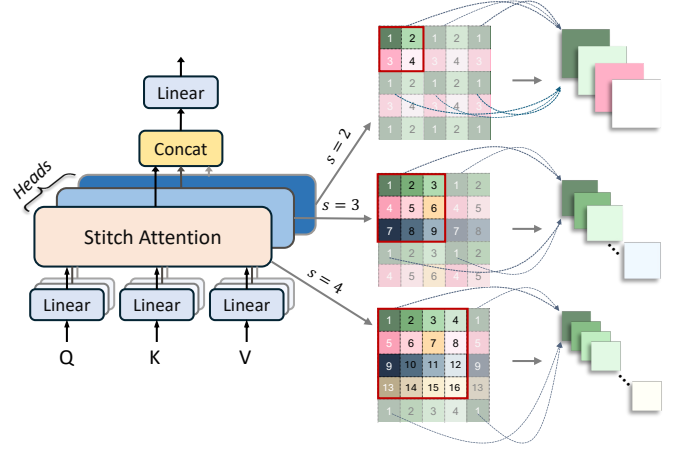


Fig. 4. Illustration of Stitch-ViT. First, the channels of the feature map are divided into different heads. Then, “stitch” operation is performed to sample the feature map using different stitch rates in different heads. Finally, the sampled feature maps are concatenated and transformed to the original feature map. The red box highlights the stitch rates of our method, and the blue points reveal the sampling positions.

rate to $s = 2, 4, 8, 16$ to obtain multi-scale feature patches with diverse receptive fields.

For instance, when considering a stitch rate of $s = 2$, the corresponding patches are obtained by sampling the feature map with a stride of 2. This process can be defined as follows:

$$\begin{aligned} P_1 &= F_c[1 :: 2, 1 :: 2, :], \\ P_2 &= F_c[1 :: 2, 2 :: 2, :], \\ P_3 &= F_c[2 :: 2, 1 :: 2, :], \\ P_4 &= F_c[2 :: 2, 2 :: 2, :], \end{aligned} \quad (1)$$

where P_i denotes the i -th patch, and $[a :: b]$ denotes the sampling operation with a stride of b starting from a . Subsequently, self-attention is performed on each patch to capture the long-range feature dependencies:

$$A = \text{softmax}\left(\frac{QK^T}{\sqrt{d_k}}\right)V, \quad (2)$$

where Q , K , and V are the query, key, and value matrices, respectively, which are obtained by linearly projecting the input patch embeddings as $Q = W_q P_i$. d_k is the dimension of the key. Empirically, truncating the feature vectors within a certain range does not diminish the model’s recognition performance. Instead, it can significantly reduce the computational cost (Zhang et al., 2020b). The resulting feature representation from the MHSA layer is then passed through the feed-forward network (FFN) to obtain the output F_t :

$$F_t = \text{FFN}(A), \quad (3)$$

where FFN consists of two 3×3 convolutional layers with the ReLU activation function. Finally, F_t is reshaped into the same size as F_c to obtain the output. The remaining transformer blocks are processed similarly. All outputs of the transformer blocks are concatenated along the channel dimension and fed into a 3×3 convolutional layer to obtain the final output.

StitchViT ingeniously orchestrates the assimilation of long-range dependencies by seamlessly stitching together localized features from multiple overlapping patches. Furthermore, this innovative methodology excels in harmonizing the aggregation of global insights while preserving the minutiae of local details, a critical facet in the nuanced landscape of medical image segmentation endeavors.

3.3. Boundary-Guided Decoder Network

The boundary-guided decoder network incorporates a boundary-extracted module to extract the explicit boundary information of foreground objects. The boundary-enhanced image feature F_b is then integrated into the multi-level encoder's features by a boundary-injected module. This aims to simultaneously characterize the intra- and inter-class consistency in the feature space, enriching the feature representative ability.

3.3.1. Boundary-Extracted Module (BEM)

BEM takes the high-level F_c^4 and low-level features F_c^1 as inputs to extract the boundary mask while filtering out the trivial boundary-irrelevant information. To achieve this, we employ the widely used Sobel operator (Kanopoulos et al., 1988) in both the horizontal (G_x) and vertical (G_y) directions to obtain gradient maps. Specifically, we utilize two 3×3 parameter-fixed operators with a stride of 1. The definitions of these operators are as follows:

$$K_x = \begin{bmatrix} -1 & 0 & 1 \\ -2 & 0 & 2 \\ -1 & 0 & 1 \end{bmatrix}, \quad K_y = \begin{bmatrix} -1 & -2 & -1 \\ 0 & 0 & 0 \\ 1 & 2 & 1 \end{bmatrix}. \quad (4)$$

Next, we apply these operators to the input feature map to obtain the gradient maps M_x and M_y . The gradient maps are then normalized using a sigmoid function and fused with the input feature map to yield the boundary-enhanced feature map F_e :

$$F_e = F_c \odot \sigma(M_{xy}), \quad (5)$$

where \odot denotes the element-wise multiplication operation, σ is the sigmoid activation function, and M_{xy} is the concatenation operation of M_x and M_y along the channel dimension. We proceed to fuse the edge-enhanced feature maps F_e^1 and F_e^4 using a simple stacked convolution layer in the bottleneck. Specifically, we first apply a 1×1 convolution followed by bilinear upsampling to match the size of F_e^1 . Then, we separately apply a 1×1 convolution layer to align the channel sizes of these two features. Finally, we concatenate the resulting feature maps along the channel dimension and apply a two-layer 3×3 convolution to obtain the final feature map \bar{F}_e . The output is supervised by the ground truth boundary map, which eliminates the noise in the edge features, producing the boundary-enhanced feature F_b .

3.3.2. Boundary-Injected Module (BIM)

The enhanced features generated by BEM can serve as a prior to enhance the image segmentation capability. In this regard, we propose the Boundary-injected module (BIM), which integrates the boundary-enhanced feature F_b into the decoder network. At the core of BIM lies the Boundary Injection Operation (BIO), which employs a dual-path boundary fusion scheme

to enhance the feature representation in both the foreground and background. BIO takes two inputs: the channel-wise concatenation of the boundary-enhanced feature F_b and the corresponding feature F_c from the encoder network, as well as the feature from the previous decoder layer F_d^{j-1} . These two inputs are fed into BIO, as depicted in Figure 2(c), which consists of two separate paths designed to enhance the feature representation in the foreground and background, respectively. For the foreground path, we concatenate the two inputs along the channel dimension and apply sequential *Conv-BN-ReLU* (i.e., 3×3 convolution, batch normalization, ReLU) layers to obtain the foreground feature F_{fg} . As for the background path, we incorporate a background attention component to selectively focus on the background information. This is expressed as:

$$F_{bg} = \text{Convs}((1 - \sigma(F_d^{j-1})) \odot F_c), \quad (6)$$

where *Convs* is a three-layer *Conv-BN-ReLU* layer, σ is the sigmoid function, and \odot denotes the element-wise multiplication. The term $(1 - (\sigma F_d^{j-1}))$ is the background attention map, which is computed by first applying the sigmoid function to the feature map from the previous decoder layer, generating a foreground attention map. Then, we subtract the foreground attention map to obtain the background attention map. Finally, we concatenate the foreground feature F_{fg} , the background feature F_{bg} , and the previous decoder feature F_d^{j-1} along the channel dimension to obtain the final output F_d^j .

3.4. Overall Loss Function

Intrinsically, CTO is a multi-task learning model that performs both semantic segmentation and boundary detection in an uniform recognition framework. We define the overall loss function to jointly optimize these two tasks.

3.4.1. Segmentation Loss.

Following MedISeg model is commonly used, the semantic segmentation loss is the weighted sum of cross-entropy loss \mathcal{L}_{CE} and mean intersection-over-union (mIoU) loss \mathcal{L}_{mIoU} . They are defined as follows:

$$\mathcal{L}_{CE} = -\frac{1}{N} \sum_{i=1}^N (y_i \log(\hat{y}_i) + (1 - y_i) \log(1 - \hat{y}_i)), \quad (7)$$

$$\mathcal{L}_{mIoU} = 1 - \frac{\sum_{i=1}^N (y_i * \hat{y}_i)}{\sum_{i=1}^N (y_i + \hat{y}_i - y_i * \hat{y}_i)}, \quad (8)$$

where y_i and \hat{y}_i are the ground truth and predicted label for the i -th pixel, respectively, and N is the total number of pixels in the image.

3.4.2. Boundary Loss.

To avoid the occurrence of class imbalance between foreground and background pixels in boundary detection, we also employ the Dice Loss:

$$\mathcal{L}_{Dice} = 1 - \frac{2 \sum_{i=1}^N (y_i * \hat{y}_i)}{\sum_{i=1}^N (y_i + \hat{y}_i)}. \quad (9)$$

3.4.3. Total Loss.

The total loss is composed of the major segmentation loss \mathcal{L}_{seg} and boundary loss \mathcal{L}_{bnd} . For the boundary detection loss, we only consider the prediction from BEM, which takes encoder's feature maps from the high-level layer (*i.e.*, F_b^4) and low-level layer (*i.e.*, F_b^1) as input. As for the major image segmentation loss, we apply the deep supervision strategy to obtain the prediction from the decoder's feature at different levels. The total loss is formulated as:

$$\mathcal{L} = \mathcal{L}_{\text{seg}} + \mathcal{L}_{\text{bnd}} = \sum_i^L (\mathcal{L}_{\text{CE}} + \mathcal{L}_{\text{mIoU}}) + \alpha \mathcal{L}_{\text{Dice}}, \quad (10)$$

where L is the number of BIM, which is set to 3 in this work. α is the weighting factor, which is set to 3.

3.5. Discussion

In this section, we discuss the underlying motivation behind the proposed CTO. Based on the minimum redundancy maximum relevance (MRMR) principle, the feature set that is mutually and maximally dissimilar and relevant to the target holds superior feature representation ability (Peng et al., 2005) and generalizability. Formally, given a feature set $\mathcal{F} = F_1, F_2, \dots, F_n$, the MRMR principle aims to find a subset $\mathcal{S} \subset \mathcal{F}$ that maximizes the mutual information $I(\mathcal{S}; Y)$ with a response variable Y , while minimizing the redundancy $I(\mathcal{S}; \mathcal{F})$:

$$\text{MRMR}(\mathcal{F}) = \underset{\mathcal{S} \subset \mathcal{F}}{\text{argmax}} \underbrace{\frac{1}{|\mathcal{S}|} \sum_{f \in \mathcal{S}} I(F, Y)}_{\text{Relevance}} - \underbrace{\frac{1}{|\mathcal{S}|^2} \sum_{f \in \mathcal{S}} I(F, \mathcal{F})}_{\text{Redundancy}}. \quad (11)$$

In the context of CTO, our main objective is to leverage the strengths of CNN, Transformer, and the edge detection operator to achieve accurate medical image segmentation. Specifically, the CNN stream within the encoder network is designed to capture local information, while the Transformer stream focuses on capturing global information. Additionally, the edge detection operator is utilized to extract crucial boundary information of the object. The features extracted from these three modules are highly relevant to the target in the medical image segmentation task, while simultaneously exhibiting dissimilarity with each other. For instance, in the case of abdominal organ segmentation using the BTCV dataset, the CNN stream is adept at capturing contextual information pertaining to the organ surface, the Transformer stream excels at capturing global semantic information such as position, and the edge detection operator effectively highlights the contrast between the organ and its background. By combining these three modules, we can effectively enhance the feature representation capabilities of the model and improve its generalization ability, thereby facilitating accurate medical image segmentation.

4. Experiments

4.1. Datasets and Evaluation Metrics

Datasets. In our experiments, we evaluate the performance of CTO on seven publicly available MedISeg datasets, namely

ISIC 2016 (Codella et al., 2019), ISIC 2018 (Codella et al., 2019), PH2 (Mendonça et al., 2013), the Colon Nuclei Identification and Counting (CoNIC) challenge dataset (Graham et al., 2021b), the Liver Tumor Segmentation (LiTS17) challenge dataset (Bilic et al., 2023), MSD BraTS (Antonelli et al., 2022), and the Beyond the Cranial Vault (BTCV) challenge dataset (Vaswani et al., 2017). The brief introduction of these experimental datasets is as follows:

- ISIC 2016 (Codella et al., 2019) and ISIC 2018 (Codella et al., 2019) are datasets of dermoscopic lesion images for melanoma segmentation, these two datasets are available in the International Skin Imaging Collaboration (ISIC) challenge. ISIC 2016 contains 1187 images, while ISIC 2018 contains 2594 images.
- PH2 (Mendonça et al., 2013) is a dataset of dermoscopic images for melanoma detection and classification, which consists of 200 images.
- The CoNIC challenge dataset (Graham et al., 2021b) is a collection of colon tissue images for nuclei segmentation and counting, which contains 4,981 non-overlapping image patches of size 256×256 .
- The LiTS17 challenge dataset (Bilic et al., 2023) is a collection of abdominal CT scans for liver tumor segmentation, which contains 130 training and 70 testing cases.
- MSD BraTS (Antonelli et al., 2022) consists of 484 MRI scans of brain tumor, with four modalities: FLAIR, T1w, T1gd, and T2w.
- The BTCV dataset (Vaswani et al., 2017) is a collection of abdominal CT scans for organ segmentation. We use the 30 abdominal CT scans in the MICCAI 2015 Multi-Atlas Abdomen Labeling Challenge, with 3779 axial contrast-enhanced abdominal clinical CT images in total.

On the datasets of ISIC 2018, CoNIC, and LiTS17 datasets, we perform 5-fold cross-validation. We use ISIC 2016 as our training dataset and employ PH2 as our independent test set to assess the generalizability of the model. MSD BraTS is divided into 80%, 15%, and 5% for training, validation, and test. For BTCV, we follow the approach of previous studies (Cao et al., 2021; Chen et al., 2024) and split the dataset into 18 cases for training and 12 cases for testing.

Evaluation Metrics. We employ commonly used evaluation metrics in MedISeg, including Dice Coefficient (Dice), Intersection over Union (IoU), average Hausdorff Distance (HD), and Panoptic Quality (PQ) (Cao et al., 2021; Chen et al., 2024; Lee et al., 2020). Additionally, we evaluate the model efficiency using the number of Floating-point Operations (FLOPs) and model Parameters (Params.). These metrics provide a comprehensive evaluation of the segmentation performance and computational efficiency of our proposed method.

4.2. Baseline Models

4.3. Implementation Details

The proposed CTO is optimized using the Adam optimizer with an initial learning rate of $1e-4$. The batch size is set to 32,

Table 1. Result comparisons (%) on ISIC 2018 for selecting of the encoder network. “w/” denotes with the corresponding module implementation.

Methods	Dice↑	IoU↑	GFLOPs↓	Params↓	Memory↓
CNNs-ViT					
TransUNet	89.97	83.30	37.02	114.65	7302
TransFuse	89.62	82.89	63.84	71.27	6914
MedFormer	89.15	82.19	21.02	80.44	5564
LeViT	86.98	79.66	23.57	64.23	6734
Sequential (Res2Net + StitchViT)	89.86	83.02	20.67	154.25	5492
Parallel (Res2Net + StitchViT)	90.63	83.97	22.70	62.22	4104
CNNs-based (+StitchViT)					
ResNet	90.28	83.63	31.10	61.66	3984
ResNeXt	89.53	82.76	22.35	61.13	4020
Res2NeXt	90.42	83.82	22.28	60.78	4098
Res2Net	90.63	83.97	22.70	62.22	4104
Transformer-based (+Res2Net)					
ViT	90.38	83.79	22.70	61.82	4022
SwinV2	90.30	83.77	23.13	62.04	7458
FasterViT	90.22	83.62	22.83	62.32	5568
Twins	90.18	83.59	23.47	62.37	9778
StitchViT	90.63	83.97	22.70	62.22	4104

and the input image size was 256×256 . The encoder network is initialized with the pre-trained weights of Res2Net-50 (Gao et al., 2019) on ImageNet (Deng et al., 2009) and then fine-tuned for 90 epochs on a single NVIDIA RTX 3090 GPU. All 3D volumes are inferred in a sliding-window manner with a stride of 1 in the z -axis direction, and the final segmentation results are obtained by stacking the prediction maps to reconstruct the 3D volume for evaluation. Except for a special statement, all experimental settings, including data pre-processing procedures, follows the previous paper (Cao et al., 2021; Lee et al., 2020). The experimental design is carefully planned to ensure that the proposed CTO is optimized and evaluated under rigorous conditions.

4.4. Ablation Study

Our ablation study aims to explore the effectiveness of each component (*i.e.*, dual-stream encoder, CBM, BEM, and BIM) in CTO and demonstrate the superiority of boundary-guided decoder. To achieve these goals, we add different components to the baseline model, and compared boundary-guided decoder with the state-of-the-art (SOTA) boundary detection methods currently used for MedISeg.

Effectiveness of Dual-Stream Encoder. In this section, we conduct an experimental analysis to assess the feature extraction capabilities of different encoders. The results are presented in Table 1. First, on the ISIC 2018 dataset, we compare our dual-stream encoder with SOTA hybrid encoders that combine CNNs and Transformers, including TransUNet (Chen et al., 2024), TransFuse (Zhang et al., 2021b), MedFormer (Gao et al., 2022), LeViT (Graham et al., 2021a). Notably, our dual-stream encoder achieves the highest performance with a Dice score of 90.63% and an IoU score of 83.97%, surpassing the performance of the other methods.

Furthermore, in order to evaluate the individual effectiveness of the CNNs and Transformers within the dual-stream

Table 2. Result comparisons (%) on ISIC 2016 (Codella et al., 2019) for validating the superiority of our boundary enhanced module. “w/” denotes with the corresponding module implementation.

Settings	Dice ↑	IoU ↑	GFLOPs↓
Baseline	91.59	84.92	17.13
w/ BATR (Wang et al., 2021)	91.62	85.03	45.99
w/ XBound-Former (Wang et al., 2023)	92.11	86.07	20.84
w/ PEE (Wang et al., 2022)	91.12	84.65	23.45
w/ Boundary Loss (Kervadec et al., 2019)	91.75	85.25	17.13
w/ Boundary DoU Loss (Sun et al., 2023)	92.01	85.70	17.13
w/ BEM (ours)	92.56	86.60	22.70

Table 3. Ablation study results (%) on ISIC 2018 (Codella et al., 2019). We choose Res2Net (Gao et al., 2019) and a lightweight ViT (Dosovitskiy et al., 2020) as the baseline models. “*” means the component achieves significant performance improvement with $p < 0.05$ via paired t-test.

CNNs	Stitch-ViT	CBM	BEM	BIM	Dice ↑	IoU ↑
✓	✗	✗	✗	✗	89.18	82.46
✗	✓	✗	✗	✗	87.53	79.89
✓	✓	✗	✗	✗	89.60* _{+0.42}	82.92* _{+0.46}
✓	✓	✓	✗	✗	89.74* _{+0.56}	83.03* _{+0.57}
✓	✓	✓	✓	✗	90.19* _{+1.01}	83.56* _{+1.10}
✓	✓	✓	✓	✓	90.63* _{+1.45}	83.97* _{+1.51}

encoder, we conduct additional experiments by substituting Res2Net (Gao et al., 2019) with ResNet (He et al., 2016), ResNeXt (Xie et al., 2017), and Res2NeXt (Gao et al., 2019), and replacing StitchViT with ViT (Dosovitskiy et al., 2020), SwinV2 (Liu et al., 2022), FasterViT (Hatamizadeh et al., 2024), and Twins (Chu et al., 2021). We also compare our dual-stream encoder with the sequential encoder, where the CNNs and Transformers are concatenated in a sequential manner. The results presented in Table 1 demonstrate the consistent superiority of our dual-stream encoder compared to other methods. This reaffirms the effectiveness of our dual-stream encoder in capturing both local and global information, thereby enhancing its performance in the context of MedISeg.

Superiority of Boundary-Guided Decoder. We have carefully selected SOTA boundary-enhanced MedISeg methods to compare with our boundary-guided decoder. These methods include BATR (Wang et al., 2021), XBound-Former (Wang et al., 2023), PEE (Wang et al., 2022), Boundary Loss (Kervadec et al., 2019), and Boundary DoU Loss (Sun et al., 2023). Specifically, we deployed different boundary detection methods on the same baseline model (*i.e.*, CNNs + StitchViT), and the experimental results are shown in Table 2. Notably, the incorporation of these boundary detection methods into the baseline model proves beneficial in further improving the overall performance of the model. This emphasizes the significance of incorporating boundary information in the context of MedISeg.

Furthermore, our CTO demonstrates the most significant performance improvement compared to the other methods, while maintaining a comparable increase in computational overheads. This not only highlights the effectiveness of the CTO, but also

Table 4. Result comparisons (%) with the state-of-the-art methods on ISIC (Gutman et al., 2016; Codella et al., 2019) & PH2 (Mendonça et al., 2013). “Nan” denotes that this model is based on shallow learning and does not have a backbone.

Methods	Backbone	ISIC 2016 & PH2		Methods	Backbone	ISIC 2018	
		Dice ↑	IoU ↑			Dice ↑	IoU ↑
SSLS (Ahn et al., 2015)	Nan	78.38	68.16	Deeplabv3 (Chen et al., 2017)	ResNet-50	88.4	80.6
MSCA (Bi et al., 2016)	Nan	81.57	72.33	U-Net++ (Zhou et al., 2018)	VGG-16	87.9	80.5
FCN (Long et al., 2015)	VGG-16	89.40	82.15	CE-Net (Gu et al., 2019)	ResNet-34	89.1	81.6
MFCN (Bi et al., 2017)	VGG-16	90.66	83.99	MedT (Valanarasu et al., 2021)	ViT-B16	85.9	77.8
SBPSeg (Lee et al., 2020)	VGG-16	<u>91.84</u>	<u>84.30</u>	TransUNet (Chen et al., 2024)	ResNet-50	<u>89.4</u>	<u>82.2</u>
MedSAM (Ma et al., 2024)	ViT-B16	84.67	78.20	MedSAM (Ma et al., 2024)	ViT-B16	83.5	77.4
CTO(Ours)	CNNs-ViT	92.56	86.60	Ours	CNNs-ViT	90.6	84.0

Table 5. Result comparisons (%) with the state-of-the-art methods on CoNIC (Graham et al., 2021b) and LiTS17 (Bilic et al., 2023).

Methods	Backbone	CoNIC			LiTS17		Complexity		
		Dice ↑	IoU ↑	PQ ↑	Dice ↑	IoU ↑	Params.(M)	GFLOPs	Memory(MB)
V-Net (Milletari et al., 2016)	ResNet-50	78.39 _{3.397}	65.15 _{4.287}	62.12 _{7.660}	82.63 _{0.420}	70.79 _{0.669}	11.84	18.54	3452
U-Net (Ronneberger et al., 2015)	VGG-16	79.70 _{1.388}	67.25 _{1.798}	66.09 _{2.299}	79.50 _{2.111}	66.64 _{2.738}	7.78	14.59	3506
R50-UNet (Ronneberger et al., 2015)	ResNet-50	78.79 _{2.003}	65.85 _{2.872}	64.31 _{4.129}	86.09 _{3.304}	76.02 _{5.041}	33.69	20.87	6524
Att-UNet (Schlemper et al., 2019)	VGG-16	<u>80.09</u> _{1.372}	<u>67.55</u> _{1.750}	<u>66.79</u> _{2.091}	79.68 _{2.063}	66.67 _{2.823}	7.88	43.35	2948
R50-AttUNet (Schlemper et al., 2019)	ResNet-50	78.33 _{2.661}	65.24 _{3.442}	63.40 _{4.825}	85.91 _{3.017}	76.30 _{3.401}	33.25	49.25	3546
R50-ViT (Dosovitskiy et al., 2020)	ResNet-50	75.25 _{1.229}	60.97 _{1.486}	56.91 _{2.316}	77.87 _{1.036}	64.39 _{1.427}	110.62	26.91	8622
UNETR (Hatamizadeh et al., 2022b)	ViT-B16	74.48 _{3.772}	60.13 _{4.532}	54.60 _{7.829}	77.83 _{0.617}	64.10 _{0.748}	87.51	26.41	6004
Swin-UNETR (Hatamizadeh et al., 2022a)	Swin-T	75.19 _{2.784}	60.92 _{3.274}	56.93 _{5.573}	75.03 _{1.805}	60.35 _{2.326}	6.29	4.86	4616
MedSAM (Ma et al., 2024)	ViT-B16	73.84 _{3.188}	59.13 _{3.814}	54.78 _{6.200}	<u>86.44</u> _{1.428}	<u>76.55</u> _{2.121}	93.74	28.56	6644
CTO (Ours)	CNNs-ViT	80.68 _{1.578}	67.97 _{2.113}	67.17 _{2.466}	88.98 _{1.901}	80.55 _{3.003}	62.22	22.70	4104

Table 6. Result comparisons (%) with the state-of-the-art methods on BTCV (Irshad et al., 2023).

Methods	mDice ↑	HD ↓	Aorta	Gallbladder	Kidney(L)	Kidney(R)	Liver	Pancreas	Spleen	Stomach
V-Net (Milletari et al., 2016)	68.81	-	75.34	51.87	77.10	80.75	87.84	40.05	80.56	56.98
DARR (Fu et al., 2020)	69.77	-	74.74	53.77	72.31	73.24	94.08	54.18	89.90	45.96
U-Net (Ronneberger et al., 2015)	76.85	39.70	89.07	69.72	77.77	68.60	93.43	53.98	86.67	75.58
R50-UNet (Ronneberger et al., 2015)	74.68	36.87	84.18	62.84	79.19	71.29	93.35	48.23	84.41	73.92
Att-UNet (Schlemper et al., 2019)	77.77	36.02	89.55	<u>68.88</u>	77.98	71.11	93.57	58.04	87.30	75.75
R50-AttUNet (Schlemper et al., 2019)	75.57	36.97	55.92	63.91	79.20	72.71	93.56	49.37	87.19	74.95
R50-ViT (Dosovitskiy et al., 2020)	71.29	32.87	73.73	55.13	75.80	72.20	91.51	45.99	81.99	73.95
TransUNet (Chen et al., 2024)	77.48	31.69	87.23	63.13	81.87	77.02	94.08	55.86	85.08	75.62
SwinUNet (Cao et al., 2021)	79.12	21.55	85.47	66.53	83.28	79.61	94.29	56.58	90.66	76.60
UNETR++ (Shaker et al., 2024)	84.54	17.89	90.65	68.64	87.59	87.00	95.64	74.58	<u>90.70</u>	<u>81.48</u>
MedSAM (Ma et al., 2024)	68.04	-	53.62	61.87	72.86	67.96	77.55	<u>69.36</u>	73.01	69.10
CTO(Ours)	<u>80.94</u>	<u>19.45</u>	86.72	64.68	<u>84.56</u>	<u>80.82</u>	<u>95.01</u>	61.66	90.88	83.16

underscores its efficiency in terms of computational resources.

Effectiveness of Each Component. In this study, we conduct an extensive experimental analysis to compare the performance of various variants of CTO on the ISIC 2018 dataset, as documented in Codella et al. (2019). The evaluated variants encompass CNNs, StitchViT, CBM, BEM, and BIM. CBM indicates the convolutional boundary module, which is specifically designed to extract boundary features without employing the Sobel operator. Our results, presented in Table 3, unequivocally demonstrate the substantial performance enhancements that each of these components can offer over the baseline model. Notably, when incorporated into the CNNs-based baseline, the +StitchViT, +CBM, +BEM, and +BIM variants yield

Dice score improvements of 0.42%, 0.56%, 1.01%, and 1.45%, respectively. Additionally, these components exhibit improvements in IoU performance, with gains of 0.46%, 0.57%, 1.10%, and 1.57% on the CNNs-based baseline, respectively. These compelling findings underscore the effectiveness of the evaluated CTO variants in enhancing the segmentation performance of the baseline model.

Furthermore, our results reveal that the addition of a CNNs model atop StitchViT yields superior performance compared to ViT alone. This observation suggests that the fusion of different models can yield enhanced performance compared to relying on a single model. Of particular importance, our findings highlight the remarkable improvement achieved by the BIM variant,

Table 7. Result comparisons (%) with the state-of-the-art methods on MSD BraTS (Antonelli et al., 2022).

Method	Mean		WT		ET		TC	
	HD ↓	Dice ↑	HD ↓	Dice ↑	HD ↓	Dice ↑	HD ↓	Dice ↑
V-Net (Milletari et al., 2016)	7.50	76.38	7.16	83.06	8.43	71.13	6.92	74.94
U-Net (Ronneberger et al., 2015)	5.82	83.33	6.25	90.09	4.59	78.18	6.62	81.73
R50-UNet (Ronneberger et al., 2015)	5.47	83.10	5.50	90.08	4.71	78.04	6.22	81.18
Att-UNet (Schlemper et al., 2019)	5.80	83.08	6.70	89.98	4.99	77.53	5.74	81.75
R50-AttUNet (Schlemper et al., 2019)	6.81	83.11	5.80	90.47	7.58	76.42	7.06	82.44
R50-ViT (Dosovitskiy et al., 2020)	5.95	82.82	5.45	89.72	5.50	77.13	6.91	81.59
TransUNet (Chen et al., 2024)	5.43	83.63	4.93	<u>90.55</u>	4.96	77.90	6.30	82.42
SwinUNet (Cao et al., 2021)	5.12	<u>84.10</u>	5.61	90.38	3.53	79.87	6.23	<u>82.57</u>
MedSAM (Ma et al., 2024)	6.30	80.58	6.74	89.57	5.46	71.55	6.70	80.62
CTO (ours)	<u>5.42</u>	84.62	6.43	90.76	<u>4.56</u>	<u>79.77</u>	5.27	83.33

with a notable increase of 1.45% in Dice score and 1.51% in IoU score. This observation emphasizes the pivotal role played by BIM in enhancing segmentation performance in the realm of medical imaging applications. The results presented in this ablation study unequivocally demonstrate the substantial improvements in baseline performance achieved by the evaluated CTO variants on the ISIC 2018 dataset. These findings underscore the significance of these components in improving performance in medical imaging applications and suggest that well-designed combinations of different models can lead to further advancements in performance.

4.5. Comparisons with State-of-the-Arts

To demonstrate the exceptional performance and versatility of our proposed CTO, we conduct comparisons with SOTA methods on various MedISeg benchmarks encompassing different modalities, including dermatologic images (*i.e.*, ISIC 2016 (Gutman et al., 2016), PH2 (Mendonça et al., 2013), and ISIC 2018 (Codella et al., 2019)), histopathological images (CoNIC (Graham et al., 2021b)), and radiological images (LiTS17 (Bilic et al., 2023), MSD BraTS (Antonelli et al., 2022), and BTCV (Vaswani et al., 2017)).

On the ISIC 2016 and PH2 datasets, we compare our CTO with five related methods, namely, SSLS (Ahn et al., 2015), MSCA (Bi et al., 2016), FCN (Long et al., 2015), MFCN (Bi et al., 2017), and SBPSeg (Lee et al., 2020). The results, presented in Table 4, exhibit notable achievements by our CTO, surpassing the previous SOTA SBPSeg (Lee et al., 2020) by 0.72% and 2.30% in Dice and IoU scores, respectively, with an outstanding performance of 92.56% in Dice and 86.60% in IoU. On the ISIC 2018 dataset, our CTO achieves remarkable results with 90.6% in Dice and 84.0% in IoU through 5-fold cross-validation. These scores outperform the SOTA TransUNet (Chen et al., 2024) by 1.2% and 1.8%, respectively, further demonstrating the robust learning capacity and generalizability of our proposed CTO. These results also underscore the pivotal role of boundary information in lesion segmentation.

Moving on to the CoNIC dataset, our CTO consistently outperforms other methods through five-fold cross validation, as evidenced by the results presented on the left side of Table 5. Notably, our method excels over the current SOTA Att-UNet (Schlemper et al., 2019) by 0.59% in Dice, 0.42% in IoU,

and 0.38% in PQ, respectively. These compelling results on ISIC 2016, PH2, ISIC 2018, and CoNIC validate the superiority of our method in the realm of 2D medical image segmentation tasks.

In addition to the 2D MedISeg, we have also conducted experiments on 3D MedISeg, utilizing the LiTS17, MSD BraTS, BTCV datasets. On LiTS17, as depicted on the right side of Table 5, our method achieves an average of 88.98% in Dice and 80.55% in IoU across five folds, surpassing the second-best performing method, R50-UNet (Ronneberger et al., 2015) by 2.89% and 4.53%, respectively. On MSD BraTS, our CTO achieves an average Dice score of 84.62%, outperforming the second-best performing method, SwinUNet(Cao et al., 2021), by 0.52%. In terms of HD, our method achieves an average of 5.42 mm, positioning it as the second-best performer among the compared methods.

Turning our attention to BTCV, as presented in Table 6, our proposed CTO achieves remarkable Dice scores of 80.94%, ranking the second-best performance among the methods. Particularly noteworthy is the significant improvement observed for organs with blurry boundaries, such as “spleen” and “stomach,” where our model achieves gains of 0.18% and 1.68% in Dice, respectively. Our method is inferior to the UNETR++ in the task of 3D organ segmentation, we believe that the performance of our method can be further improved by extending the model to a 3D version. Moreover, our CTO exhibits competitive performance improvements while upholding a comparable computational load. The final model configuration of CTO comprises 62.22M parameters, 22.70G FLOPs, and 4104 MB of GPU memory.

4.6. Statistical Analysis

To compare the disparities between our methodology and the current leading methods, we conduct a statistical significance analysis using the paired t-test with the Bonferroni correction. The results are visually represented with bars atop the box plots, where significance levels are denoted as follows: non-significant (*ns*, $p > 0.05$), significant: * ($0.01 < p < 0.05$), ** ($0.001 < p < 0.01$), *** ($p < 0.001$). The statistical analysis outcomes are illustrated in Fig. 8.

Across the ISIC 2018, CoNIC, and LiTS datasets, our approach demonstrates a significant superiority over the second-

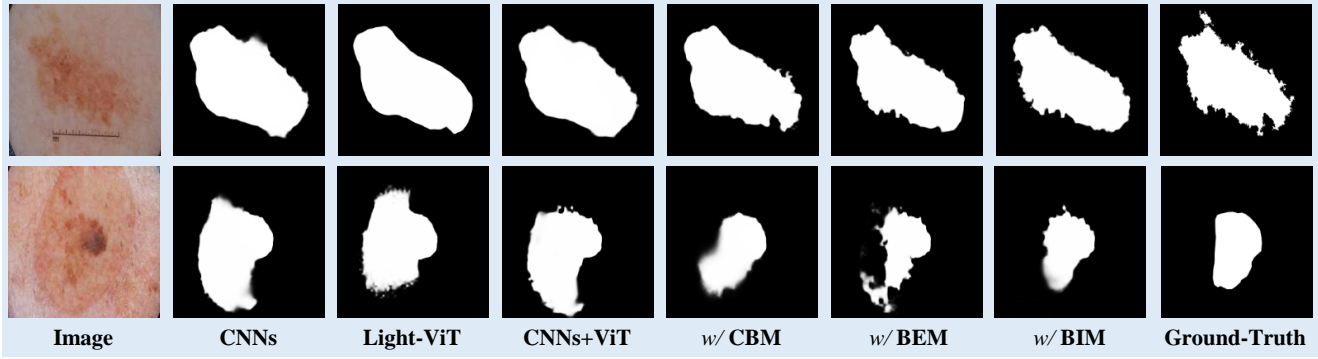


Fig. 5. Visualized results of the ablation study on ISIC 2018 Codella et al. (2019). “w/” denotes with the corresponding module implementation.

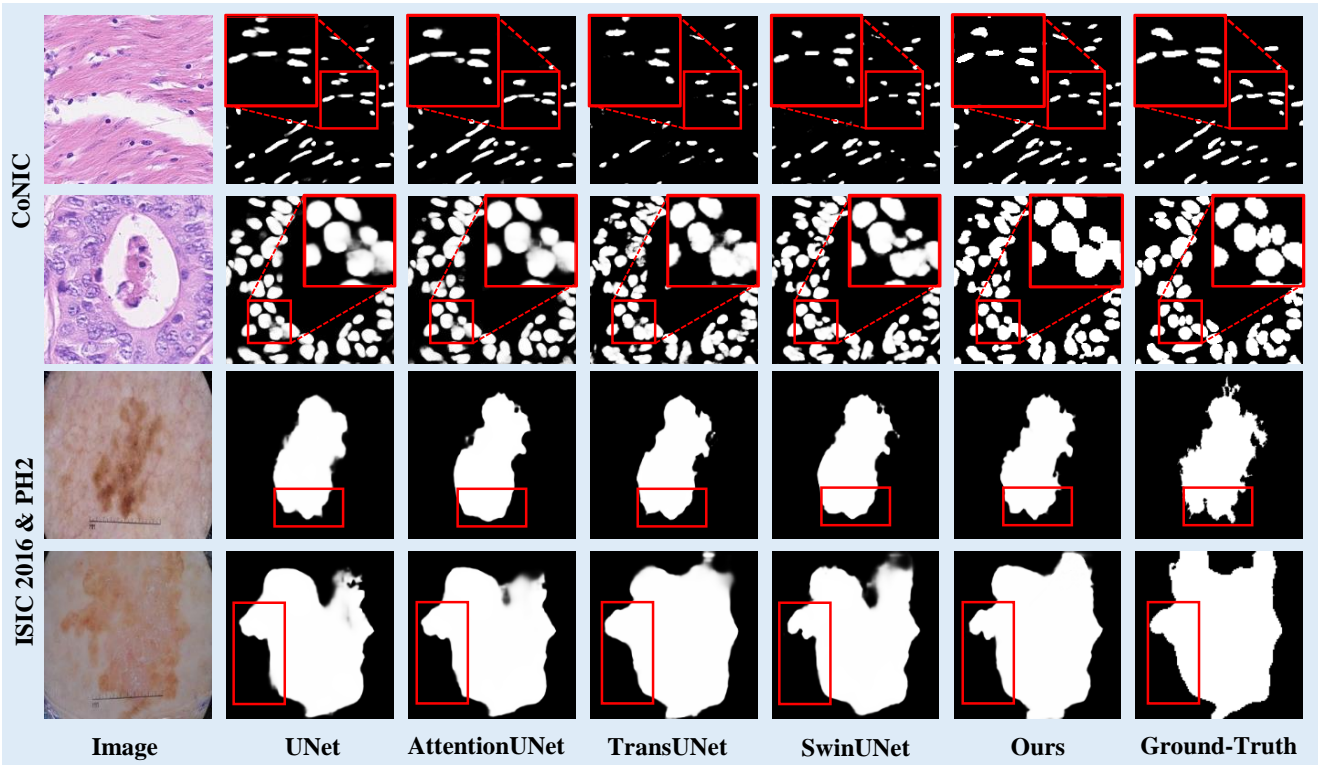


Fig. 6. Visualizations on CoNIC Graham et al. (2021b) and ISIC 2016 Gutman et al. (2016)&PH2 Mendonça et al. (2013). The red frames highlight the improved regions.

best methods (TransUNet, Attention UNet, and MedSAM). Notably, on the BTCV dataset, our method exhibits a remarkable enhancement in the Dice score, increasing from 77.77% to 80.94% when compared to the third-best performing method (Attention UNet). Furthermore, in terms of HD, CTO showcases a substantial decrease from 36.02 to 19.45 when juxtaposed with the fourth-best performing method (Attention UNet). These findings affirm that CTO consistently enhances performance significantly across all datasets compared to the majority of state-of-the-art methods.

4.7. Comparisons with Large Vision Models

Recently, the emergence of large vision models trained on extensive medical image datasets has garnered significant attention and is being hailed as the future direction for MedISeg. In light of this, in this section, we compare our method with the

large vision model in medical images, namely, Segment Anything in Medical Images (MedSAM) (Ma et al., 2024).

Examining the rows labeled “MedSAM” in Table 4 to Table 6, our method consistently outperforms MedSAM on specific datasets. Moreover, our CTO exhibits the potential for fewer parameters and more lightweight computations in comparison to MedSAM. This observation suggests that while MedSAM may possess robust learning capabilities, its performance on specific datasets remains unsatisfactory. Therefore, it is worth considering the development of more efficient and effective dataset-specific models by combining the downstream application of large MedSAM models on specific datasets.

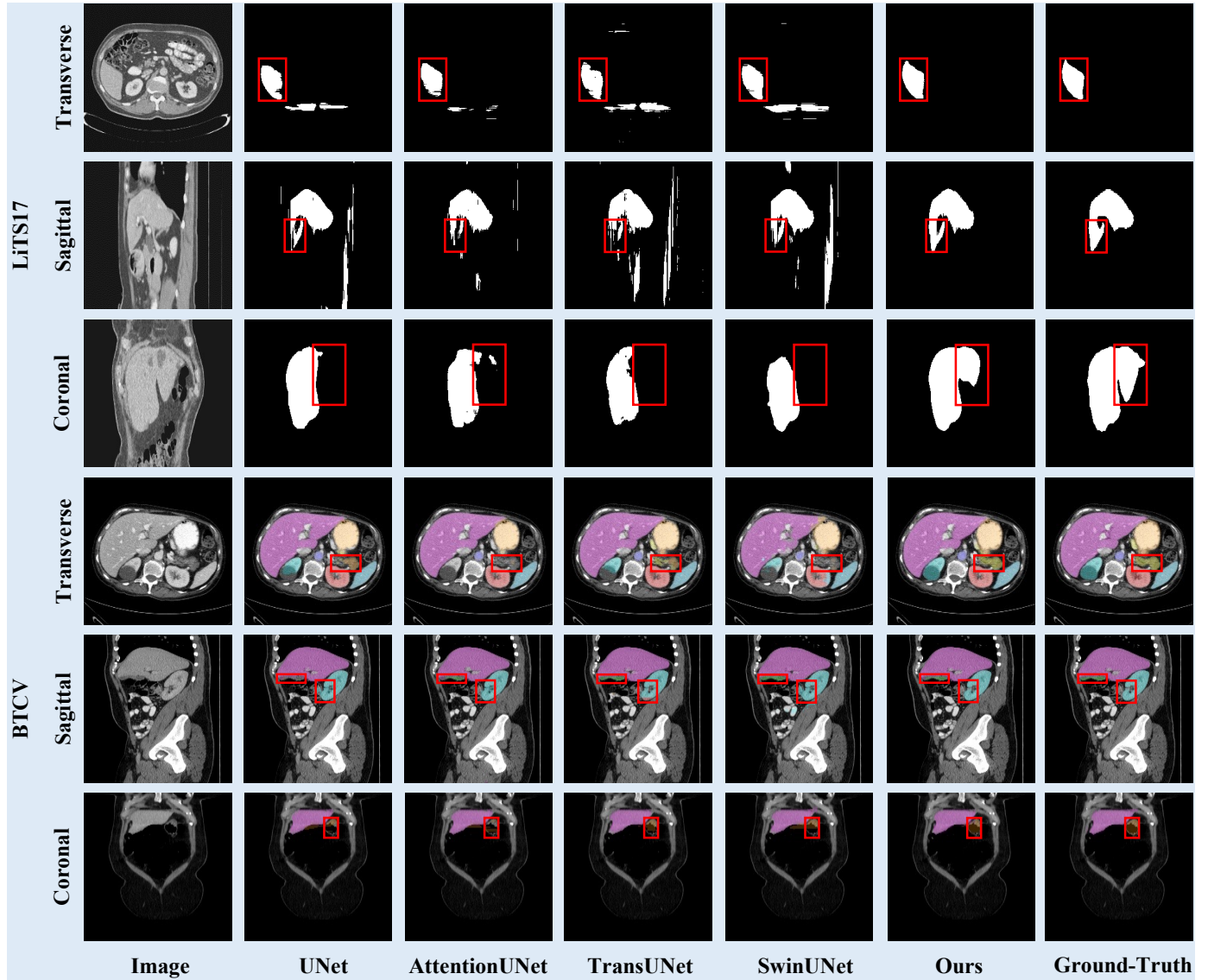


Fig. 7. Visualizations on LiTS17 Bilic et al. (2023) and BTCV Vaswani et al. (2017) in transverse, sagittal, and coronal plane. The red frames highlight the improved regions.

5. Qualitative Results

5.1. Comparisons with the Baseline Model.

The primary objective of this study is to investigate the performance of various models on the ISIC 2018 dataset (Codella et al., 2019). Specifically, we aim to evaluate the efficacy of CNNs, StitchViT, and their combination, as well as the impact of incorporating CBM, BEM, and BIM into the combined model. Our results, as depicted in Figure 5, unequivocally demonstrate that CNN-based models excel at capturing local information pertaining to foreground objects. Conversely, ViT-based models excel at retrieving global information related to foreground objects. However, both of these models exhibit the drawback of incomplete and imprecise object boundaries. On the other hand, the CNNs+ViT approach not only effectively captures local object information to enhance the smoothness of local masks but also ensures the overall completeness of objects. Furthermore, our results highlight that the addition of

CBM, BEM, and BIM to the CNNs+ViT model yields a significant improvement in both boundary delineation and object completeness. This finding underscores the crucial role played by the explicit boundary features learned by our model in the segmentation of foreground objects. Overall, the experimental results demonstrate the effectiveness of the evaluated models and emphasize the significance of integrating explicit boundary features to enhance segmentation in medical imaging applications.

5.2. Comparisons with State-of-the-Arts.

Figure 6 provides qualitative comparisons of the results on the CoNIC (Graham et al., 2021b) and ISIC 2016 (Gutman et al., 2016) & PH2 (Mendonça et al., 2013), showcasing the effectiveness of our proposed CTO method. Our results demonstrate the remarkable ability of our CTO method to accurately delineate object contours, particularly for nuclei with diverse shapes and sizes, and even for nuclei objects with blurred

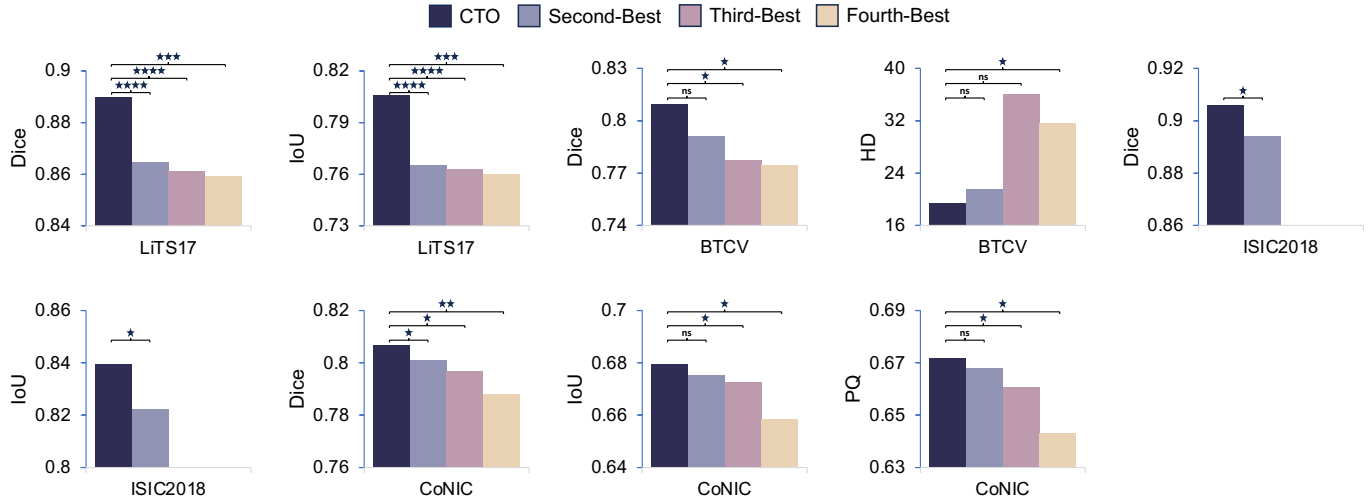


Fig. 8. Statistical analyses in terms of each quantitative metric in the manuscript between CTO and the second-best, third-best and fourth-best performing methods in ISIC2018, BTCV, CoNIC and LiTS17. p -values are calculated using paired t-test with the Bonferroni correction and referred as follows: “ns” on the plot refers to the p -value in the range: $0.05 < p \leq 1$; * refers to the p -value in the range: $0.01 < p \leq 0.05$; ** refers to the p -value in the range: $0.001 < p \leq 0.01$; *** refers to the p -value in the range: $0.0001 < p \leq 0.001$; **** refers to the p -value in the range: $p \leq 0.0001$.

boundaries. This observation underscores the significance of incorporating boundary information to enhance segmentation performance in medical image analysis tasks.

Moreover, Figure 7 provides qualitative comparisons of the results on the LiTS17 Bilic et al. (2023) and BTCV Vaswani et al. (2017) in coronal, sagittal and transverse plane. Our results establish the superiority of our CTO method over other existing methods. For instance, in all three views of the LiTS17 dataset, our method successfully segments more comprehensive boundaries, leading to a more accurate representation of liver. Moreover, in the coronal planes of images in the BTCV dataset, CTO accurately distinguishes boundaries between the pancreas and left kidney, while other methods exhibit under-segmentation of pancreas. Similarly, in the sagittal and transverse planes of images in the BTCV dataset, CTO effectively segments more accurate boundaries of right kidney and stomach compared to other methods.

These findings provide compelling evidence for the effectiveness of our proposed method in addressing medical image segmentation challenges. The experimental results not only highlight the importance of boundary information in medical image segmentation tasks but also underscore the superiority of our CTO method in comparison to other existing methods.

6. Conclusion

In this paper, we proposed a new network architecture, named CTO, specifically tailored for medical image segmentation. The proposed architecture not only achieves a superior balance between recognition accuracy and computational efficiency but also outperforms existing advanced segmentation architectures. The primary contribution of this paper lies in the ingenious use of intermediate feature maps to synthesize a high-quality boundary supervision mask, eliminating the need for additional external information. To this end, we designed the CTO network, which seamlessly integrates three crucial components

– convolution, Transformer, and edge detection operator – into a unified framework. Through extensive experimentation on seven publicly available datasets, we provide compelling evidence of the unmatched superiority of CTO over state-of-the-art methods. Furthermore, we demonstrate the exceptional effectiveness of each individual component within our architecture. The limitations of the proposed method are as follows: 1) This study does not explore the use of 3D convolutions, which could better capture spatial relationships in volumetric data, potentially improving segmentation accuracy. 2) We did not investigate the impact of domain shift between different medical imaging centers, which can affect model generalization. 3) The proposed method is not yet fully optimized for real-time applications, which may limit its practical use in clinical settings. 4) The model does not leverage pre-trained knowledge from large models, which could enhance feature learning and overall performance. The future work will concentrate on extending the concept of a dual-stream encoder to encompass diverse advanced backbone architectures, thereby elevating the effectiveness of the proposed approach. Additionally, we aim to explore the potential adaptation of CTO to a three-dimensional framework, which holds immense promise for revolutionizing medical image analysis tasks in real-world clinical practice.

Declaration of generative AI and AI-assisted technologies in the writing process

During the preparation of this work the authors used ChatGPT 3.5 Turbo in order to improve language and readability. After using this tool, the authors reviewed and edited the content as needed and take full responsibility for the content of the publication.

References

- Ahn, E., Bi, L., Jung, Y.H., Kim, J., Li, C., Fulham, M., Feng, D.D., 2015. Automated saliency-based lesion segmentation in dermoscopic images, in: *IEEE Engineering in Medicine and Biology Society*, pp. 3009–3012. doi:10.1109/EMBC.2015.7319025.
- Antonelli, M., Reinke, A., Bakas, S., Farahani, K., Kopp-Schneider, A., Landman, B.A., Litjens, G., Menze, B., Ronneberger, O., Summers, R.M., et al., 2022. The medical segmentation decathlon. *Nature Communications* 13, 4128. doi:10.1038/s41467-022-30695-9.
- Bi, L., Kim, J., Ahn, E., Feng, D., Fulham, M., 2016. Automated skin lesion segmentation via image-wise supervised learning and multi-scale superpixel based cellular automata, in: *IEEE International Symposium on Biomedical Imaging*, pp. 1059–1062. doi:10.1109/ISBI.2016.7493448.
- Bi, L., Kim, J., Ahn, E., Kumar, A., Fulham, M., Feng, D., 2017. Dermoscopic image segmentation via multitask fully convolutional networks. *IEEE Transactions on Biomedical Engineering* 64, 2065–2074. doi:10.1109/TBME.2017.2712771.
- Bilic, P., Christ, P., Li, H.B., Vorontsov, E., Ben-Cohen, A., Kaissis, G., Sze-skin, A., Jacobs, C., Mamani, G.E.H., Chartrand, G., et al., 2023. The liver tumor segmentation benchmark (LiTS). *Medical Image Analysis* 84, 102680. doi:10.1016/j.media.2022.102680.
- Bokhovkin, A., Burnaev, E., 2019. Boundary loss for remote sensing imagery semantic segmentation, in: *International Symposium on Neural Networks*, Lecture Notes in Computer Science, 11555, Springer, pp. 388–401. doi:10.1007/978-3-030-22808-8_38.
- Burger, W., Burge, M.J., 2022. *Digital Image Processing: An Algorithmic Introduction*. Springer Nature. doi:10.1007/978-3-031-05744-1.
- Cao, H., Wang, Y., Chen, J., Jiang, D., Zhang, X., Tian, Q., Wang, M., 2021. Swin-UNet: Unet-like pure Transformer for medical image segmentation, in: *European Conference on Computer Vision Workshop*, Lecture Notes in Computer Science, vol 13803, Springer, Cham, pp. 205–218. doi:10.1007/978-3-031-25066-8_9.
- Chen, H., Dou, Q., Yu, L., Qin, J., Heng, P.A., 2018. VoxResNet: Deep voxelwise residual networks for brain segmentation from 3D MR images. *NeuroImage* 170, 446–455. doi:10.1016/j.neuroimage.2017.04.041.
- Chen, H., Qi, X., Yu, L., Heng, P.A., 2016. DCAN: deep contour-aware networks for accurate gland segmentation, in: *Proceedings of the IEEE/CVF Conference on Computer Vision and Pattern Recognition*, pp. 1487–1496. doi:10.1109/CVPR.2016.273.
- Chen, J., Mei, J., Li, X., Lu, Y., Yu, Q., Wei, Q., Luo, X., Xie, Y., Adeli, E., Wang, Y., et al., 2024. TransUNet: Rethinking the u-net architecture design for medical image segmentation through the lens of Transformers. *Medical Image Analysis* 97, 103280. doi:10.1016/j.media.2024.103280.
- Chen, L.C., Papandreou, G., Schroff, F., Adam, H., 2017. Rethinking atrous convolution for semantic image segmentation. *arXiv:1706.05587*.
- Chen, X., Dong, C., Ji, J., Cao, J., Li, X., 2021. Image manipulation detection by multi-view multi-scale supervision, in: *Proceedings of the IEEE International Conference on Computer Vision*, pp. 14185–14193. doi:10.1109/ICCV48922.2021.01392.
- Chu, X., Tian, Z., Wang, Y., Zhang, B., Ren, H., Wei, X., Xia, H., Shen, C., 2021. Twins: Revisiting the design of spatial attention in vision Transformers. *Advances in Neural Information Processing Systems* 34, 9355–9366. URL: <https://openreview.net/forum?id=5kTlVBkzSRx>.
- Codella, N., Rotemberg, V., Tschandl, P., Celebi, M.E., Dusza, S., Gutman, D., Helba, B., Kalloo, A., Liopyris, K., Marchetti, M., et al., 2019. Skin lesion analysis toward melanoma detection 2018: A challenge hosted by the international skin imaging collaboration (ISIC). *arXiv:1902.03368*.
- Deng, J., Dong, W., Socher, R., Li, L.J., Li, K., Fei-Fei, L., 2009. ImageNet: A large-scale hierarchical image database, in: *Proceedings of the IEEE/CVF Conference on Computer Vision and Pattern Recognition*, pp. 248–255. doi:10.1109/CVPR.2009.5206848.
- Dosovitskiy, A., Beyer, L., Kolesnikov, A., Weissenborn, D., Zhai, X., Unterthiner, T., Dehghani, M., Minderer, M., Heigold, G., Gelly, S., et al., 2020. An image is worth 16x16 words: Transformers for image recognition at scale, in: *International Conference on Learning Representations*, pp. 1909–1920. URL: <https://openreview.net/forum?id=YicbFdNTTy>.
- Fan, D.P., Ji, G.P., Sun, G., Cheng, M.M., Shen, J., Shao, L., 2020. Camouflaged object detection, in: *Proceedings of the IEEE/CVF Conference on Computer Vision and Pattern Recognition*, pp. 2777–2787. doi:10.1109/CVPR42600.2020.00285.
- Fu, S., Lu, Y., Wang, Y., Zhou, Y., Shen, W., Fishman, E., Yuille, A., 2020. Domain adaptive relational reasoning for 3D multi-organ segmentation, in: *International Conference on Medical Image Computing and Computer Assisted Intervention*, Lecture Notes in Computer Science, vol 12261, Springer, Cham, pp. 656–666. doi:10.1007/978-3-030-59710-8_64.
- Gao, S.H., Cheng, M.M., Zhao, K., Zhang, X.Y., Yang, M.H., Torr, P., 2019. Res2Net: A new multi-scale backbone architecture. *IEEE Transactions on Pattern Analysis and Machine Intelligence* 43, 652–662. doi:10.1109/TPAMI.2019.2938758.
- Gao, X., Jin, Y., Zhao, Z., Dou, Q., Heng, P.A., 2021. Future frame prediction for robot-assisted surgery, in: *International Conference on Information Processing in Medical Imaging*, Lecture Notes in Computer Science, vol 12729, Springer, Cham, pp. 533–544. doi:10.1007/978-3-030-78191-0_41.
- Gao, Y., Zhou, M., Liu, D., Yan, Z., Zhang, S., Metaxas, D.N., 2022. A data-scalable Transformer for medical image segmentation: architecture, model efficiency, and benchmark. *arXiv preprint arXiv:2203.00131*.
- Graham, B., El-Nouby, A., Touvron, H., Stock, P., Joulin, A., Jégou, H., Douze, M., 2021a. Levit: a vision Transformer in convnet's clothing for faster inference, in: *Proceedings of the IEEE International Conference on Computer Vision*, pp. 12259–12269. doi:10.1109/ICCV48922.2021.01204.
- Graham, S., Jahanifar, M., Vu, Q.D., Hadjigeorgiou, G., Leech, T., Snead, D., Raza, S.E.A., Minhas, F., Rajpoot, N., 2021b. CoNIC: Colon nuclei identification and counting challenge 2022. *arXiv:2111.14485*.
- Gu, Z., Cheng, J., Fu, H., Zhou, K., Hao, H., Zhao, Y., Zhang, T., Gao, S., Liu, J., 2019. CE-NET: Context encoder network for 2D medical image segmentation. *IEEE Transactions on Medical Imaging* 38, 2281–2292. doi:10.1109/TMI.2019.2903562.
- Gutman, D., Codella, N.C.F., Celebi, E., Helba, B., Marchetti, M., Mishra, N., Halpern, A., 2016. Skin lesion analysis toward melanoma detection: A challenge at the international symposium on biomedical imaging (ISBI) 2016, hosted by the international skin imaging collaboration (ISIC), in: *arXiv:1605.01397*.
- Hatamizadeh, A., Heinrich, G., Yin, H., Tao, A., Alvarez, J.M., Kautz, J., Molchanov, P., 2024. FasterViT: Fast vision Transformers with hierarchical attention, in: *International Conference on Learning Representations*, pp. 1–14. URL: <https://openreview.net/forum?id=kB4yBiNmXX>.
- Hatamizadeh, A., Nath, V., Tang, Y., Yang, D., Roth, H.R., Xu, D., 2022a. Swin UNETR: Swin Transformers for semantic segmentation of brain tumors in MRI images, in: *International Conference on Medical Image Computing and Computer Assisted Intervention Brainlesion Workshop*, pp. 272–284. doi:10.1007/978-3-031-08999-2_22.
- Hatamizadeh, A., Tang, Y., Nath, V., Yang, D., Myronenko, A., Landman, B., Roth, H.R., Xu, D., 2022b. UNETR: Transformers for 3D medical image segmentation, in: *Proceedings of the IEEE/CVF Winter Conference on Applications of Computer Vision*, pp. 574–584. doi:10.1109/WACV51458.2022.00181.
- Hatamizadeh, A., Terzopoulos, D., Myronenko, A., 2019. End-to-end boundary aware networks for medical image segmentation, in: *International Workshop on Machine Learning in Medical Imaging*, pp. 187–194. doi:10.1007/978-3-030-32692-0_22.
- He, K., Zhang, X., Ren, S., Sun, J., 2016. Deep residual learning for image recognition, in: *Proceedings of the IEEE/CVF Conference on Computer Vision and Pattern Recognition*, pp. 770–778. doi:10.1109/CVPR.2016.90.
- Huang, X., Deng, Z., Li, D., Yuan, X., 2021. Missformer: An effective medical image segmentation Transformer. *IEEE Transactions on Medical Imaging*, 1484–1494doi:10.1109/TMI.2022.3230943.
- Irshad, S., Gomes, D.P., Kim, S.T., 2023. Improved abdominal multi-organ segmentation via 3D boundary-constrained deep neural networks. *IEEE Access* 11, 35097–35110. doi:10.1109/ACCESS.2023.3264582.
- Kamgar-Parsi, B., Rosenfeld, A., 1999. Optimally isotropic laplacian operator. *IEEE Transactions on Image Processing* 8, 1467–1472. doi:10.1109/83.791975.
- Kanopoulos, N., Vasanthavada, N., Baker, R.L., 1988. Design of an image edge detection filter using the Sobel operator. *IEEE Journal of Solid-State Circuits* 23, 358–367. doi:10.1109/4.996.
- Kervadec, H., Bouchtiba, J., Desrosiers, C., Granger, E., Dolz, J., Ayed, I.B., 2019. Boundary loss for highly unbalanced segmentation, in: *International Conference on Medical Imaging with Deep Learning*, PMLR, pp. 285–296. URL: <https://proceedings.mlr.press/v102/kervadec19a.html>.
- Lee, H.J., Kim, J.U., Lee, S., Kim, H.G., Ro, Y.M., 2020. Structure boundary preserving segmentation for medical image with ambiguous boundary, in: *Proceedings of the IEEE/CVF Conference on Computer Vision and Pattern Recognition*, pp. 4817–4826. doi:10.1109/CVPR42600.2020.00487.
- Li, C., Zia, M.Z., Tran, Q.H., Yu, X., Hager, G.D., Chandraker, M., 2018.

- Deep supervision with intermediate concepts. *IEEE Transactions on Pattern Analysis and Machine Intelligence* 41, 1828–1843. doi:10.1109/TPAMI.2018.2863285.
- Lin, Y., Fang, X., Zhang, D., Cheng, K.T., Chen, H., 2025. Boosting convolution with efficient MLP-permutation for volumetric medical image segmentation. *IEEE Transactions on Medical Imaging*, 1–1doi:10.1109/TMI.2025.3530113.
- Lin, Y., Liu, L., Ma, K., Zheng, Y., 2021. Seg4reg+: Consistency learning between spine segmentation and cobb angle regression, in: *International Conference on Medical Image Computing and Computer Assisted Intervention*, Lecture Notes in Computer Science, vol 12905. Springer, Cham. pp. 490–499. doi:10.1007/978-3-030-87240-3_47.
- Lin, Y., Liu, Y., Chen, H., Yang, X., Ma, K., Zheng, Y., Cheng, K.T., 2024. LENAS: Learning-based neural architecture search and ensemble for 3-D radiotherapy dose prediction. *IEEE Transactions on Cybernetics* 54, 5795–5805. doi:10.1109/tcyb.2024.3390769.
- Lin, Y., Qu, Z., Chen, H., Gao, Z., Li, Y., Xia, L., Ma, K., Zheng, Y., Cheng, K.T., 2023a. Nuclei segmentation with point annotations from pathology images via self-supervised learning and co-training. *Medical Image Analysis* 89, 102933. doi:10.1016/j.media.2023.102933.
- Lin, Y., Su, J., Wang, X., Li, X., Liu, J., Cheng, K.T., Yang, X., 2019. Automated pulmonary embolism detection from CTPA images using an end-to-end convolutional neural network, in: *International Conference on Medical Image Computing and Computer Assisted Intervention*, Lecture Notes in Computer Science, vol 11767. Springer, Cham. pp. 280–288. doi:10.1007/978-3-030-32251-9_31.
- Lin, Y., Zhang, D., Fang, X., Chen, Y., Cheng, K.T., Chen, H., 2023b. Rethinking boundary detection in deep learning models for medical image segmentation, in: *International Conference on Information Processing in Medical Imaging*, Lecture Notes in Computer Science, vol 13939. Springer, Cham. pp. 730–742. doi:10.1007/978-3-031-34048-2_56.
- Liu, Z., Hu, H., Lin, Y., Yao, Z., Xie, Z., Wei, Y., Ning, J., Cao, Y., Zhang, Z., Dong, L., et al., 2022. Swin Transformer v2: Scaling up capacity and resolution, in: *Proceedings of the IEEE/CVF Conference on Computer Vision and Pattern Recognition*, pp. 12009–12019. doi:10.1109/CVPR52688.2022.01170.
- Long, J., Shelhamer, E., Darrell, T., 2015. Fully convolutional networks for semantic segmentation, in: *Proceedings of the IEEE/CVF Conference on Computer Vision and Pattern Recognition*, pp. 3431–3440. doi:10.1109/CVPR.2015.7298965.
- Ma, J., He, Y., Li, F., Han, L., You, C., Wang, B., 2024. Segment anything in medical images. *Nature Communications* 15, 654. doi:10.1038/s41467-024-44824-z.
- Mendonça, T., Ferreira, P.M., Marques, J.S., Marcal, A.R., Rozeira, J., 2013. PH 2-A dermoscopic image database for research and benchmarking, in: *International Conference of the IEEE Engineering in Medicine and Biology Society*, pp. 5437–5440. doi:10.1109/EMBC.2013.6610779.
- Milletari, F., Navab, N., Ahmadi, S.A., 2016. V-Net: Fully convolutional neural networks for volumetric medical image segmentation, in: *International Conference on 3D Vision*, pp. 565–571. doi:10.1109/3DV.2016.79.
- Peng, H., Long, F., Ding, C., 2005. Feature selection based on mutual information criteria of max-dependency, max-relevance, and min-redundancy. *IEEE Transactions on Pattern Analysis and Machine Intelligence* 27, 1226–1238. doi:10.1109/TPAMI.2005.159.
- Ronneberger, O., Fischer, P., Brox, T., 2015. U-Net: Convolutional networks for biomedical image segmentation, in: *International Conference on Medical Image Computing and Computer Assisted Intervention*, Lecture Notes in Computer Science, vol 9351. Springer, Cham. pp. 234–241. doi:10.1007/978-3-319-24574-4_28.
- Schlemper, J., Oktay, O., Schaap, M., Heinrich, M., Kainz, B., Glocker, B., Rueckert, D., 2019. Attention gated networks: Learning to leverage salient regions in medical images. *Medical Image Analysis* 53, 197–207. doi:10.1016/j.media.2019.01.012.
- Shaker, A.M., Maaz, M., Rasheed, H., Khan, S., Yang, M.H., Khan, F.S., 2024. UNETR++: delving into efficient and accurate 3D medical image segmentation. *IEEE Transactions on Medical Imaging*, 3377–3390doi:10.1109/TMI.2024.3398728.
- Shamshad, F., Khan, S., Zamir, S.W., Khan, M.H., Hayat, M., Khan, F.S., Fu, H., 2023. Transformers in medical imaging: A survey. *Medical Image Analysis* 88, 102802. doi:10.1016/j.media.2023.102802.
- Shi, Z., Chen, H., Zhang, D., 2023. Transformer-auxiliary neural networks for image manipulation localization by operator inductions. *IEEE Transactions on Circuits and Systems for Video Technology*, 4907–4920doi:10.1109/TCSVT.2023.32514.
- Sun, F., Luo, Z., Li, S., 2023. Boundary difference over union loss for medical image segmentation, in: *International Conference on Medical Image Computing and Computer Assisted Intervention*, Lecture Notes in Computer Science, vol 14223. Springer, Cham. pp. 292–301. doi:10.1007/978-3-031-43901-8_28.
- Valanarasu, J.M.J., Oza, P., Hacihaliloglu, I., Patel, V.M., 2021. Medical Transformer: Gated axial-attention for medical image segmentation, in: *International Conference on Medical Image Computing and Computer Assisted Intervention*, Lecture Notes in Computer Science, vol 12901. Springer, Cham. pp. 36–46. doi:10.1007/978-3-030-87193-2_4.
- Vaswani, A., Shazeer, N., Parmar, N., Uszkoreit, J., Jones, L., Gomez, A.N., Kaiser, Ł., Polosukhin, I., 2017. Attention is all you need, in: *Advances in Neural Information Processing Systems*, Curran Associates, Inc.. pp. 5998–6008. URL: <http://arxiv.org/abs/1706.03762>.
- Wang, J., Chen, F., Ma, Y., Wang, L., Fei, Z., Shuai, J., Tang, X., Zhou, Q., Qin, J., 2023. Xbound-former: Toward cross-scale boundary modeling in transformers. *IEEE Transactions on Medical Imaging* 42, 1735–1745. doi:10.1109/TMI.2023.3236037.
- Wang, J., Wei, L., Wang, L., Zhou, Q., Zhu, L., Qin, J., 2021. Boundary-aware Transformers for skin lesion segmentation, in: *International Conference on Medical Image Computing and Computer Assisted Intervention*, Lecture Notes in Computer Science, vol 12901. Springer, Cham. pp. 206–216. doi:10.1007/978-3-030-87193-2_20.
- Wang, R., Chen, S., Ji, C., Fan, J., Li, Y., 2022. Boundary-aware context neural network for medical image segmentation. *Medical Image Analysis* 78, 102395. doi:10.1016/j.media.2022.102395.
- Wang, X., 2007. Laplacian operator-based edge detectors. *IEEE Transactions on Pattern Analysis and Machine Intelligence* 29, 886–890. doi:10.1109/TPAMI.2007.1027.
- Wijeratne, P.A., Alexander, D.C., Initiative, A.D.N., et al., 2021. Learning transition times in event sequences: The temporal event-based model of disease progression, in: *International Conference on Information Processing in Medical Imaging*, Lecture Notes in Computer Science, vol 12729. Springer, Cham. pp. 583–595. doi:10.1007/978-3-030-78191-0_45.
- Wu, J., Fang, H., Shang, F., Yang, D., Wang, Z., Gao, J., Yang, Y., Xu, Y., 2022. SeATrans: Learning segmentation-assisted diagnosis model via Transformer, in: *International Conference on Medical Image Computing and Computer Assisted Intervention*, Lecture Notes in Computer Science, vol 13432. Springer, Cham. pp. 677–687. doi:10.1007/978-3-031-16434-7_65.
- Xiao, H., Li, L., Liu, Q., Zhu, X., Zhang, Q., 2023. Transformers in medical image segmentation: A review. *Biomedical Signal Processing and Control* 84, 104791. doi:https://doi.org/10.1016/j.bspc.2023.104791.
- Xie, S., Girshick, R., Dollár, P., Tu, Z., He, K., 2017. Aggregated residual transformations for deep neural networks, in: *Proceedings of the IEEE/CVF Conference on Computer Vision and Pattern Recognition*, pp. 1492–1500. doi:10.1109/CVPR.2017.634.
- Yan, X., Tang, H., Sun, S., Ma, H., Kong, D., Xie, X., 2022. After-UNet: Axial fusion Transformer Unet for medical image segmentation, in: *Proceedings of the IEEE/CVF Winter Conference on Applications of Computer Vision*, pp. 3971–3981. doi:10.1109/WACV51458.2022.00333.
- Yu, C., Helwig, E.J., 2022. The role of AI technology in prediction, diagnosis and treatment of colorectal cancer. *Artificial Intelligence Review*, 323–343doi:10.1007/s10462-021-10034-y.
- Yuan, F., Zhang, Z., Fang, Z., 2023. An effective CNN and Transformer complementary network for medical image segmentation. *Pattern Recognition* 136, 109228. doi:10.1016/j.patcog.2022.109228.
- Zhang, D., Lin, Y., Chen, H., Tian, Z., Yang, X., Tang, J., Cheng, K.T., 2022a. Understanding the tricks of deep learning in medical image segmentation: Challenges and future directions. *arXiv preprint arXiv:2209.10307*.
- Zhang, D., Tang, J., Cheng, K.T., 2022b. Graph reasoning Transformer for image parsing, in: *International Conference on Multimedia*, pp. 2380–2389. doi:10.1145/3503161.354785.
- Zhang, D., Zhang, H., Tang, J., Hua, X.S., Sun, Q., 2020a. Causal intervention for weakly-supervised semantic segmentation, in: *Advances in Neural Information Processing Systems*, pp. 655–666.
- Zhang, D., Zhang, H., Tang, J., Hua, X.S., Sun, Q., 2021a. Self-regulation for semantic segmentation, in: *Proceedings of the IEEE International Conference on Computer Vision*, pp. 6953–6963. doi:10.1109/ICCV48922.2021.00687.

- Zhang, D., Zhang, H., Tang, J., Wang, M., Hua, X., Sun, Q., 2020b. Feature pyramid transformer, in: Computer Vision–ECCV 2020: 16th European Conference, Glasgow, UK, August 23–28, 2020, Proceedings, Part XXVIII 16, Springer. pp. 323–339. doi:10.1007/978-3-030-58604-1_20.
- Zhang, D., Zhang, L., Tang, J., 2023. Augmented FCN: rethinking context modeling for semantic segmentation. *Science China Information Sciences* 66, 142105. doi:10.1007/s11432-021-3590-1.
- Zhang, Y., Liu, H., Hu, Q., 2021b. Transfuse: Fusing Transformers and CNNs for medical image segmentation, in: International Conference on Medical Image Computing and Computer Assisted Intervention, Lecture Notes in Computer Science, vol 12901. Springer, Cham. pp. 14–24. doi:10.1007/978-3-030-87193-2_2.
- Zhao, W., Zhong, L., Wang, G., 2024. SEMI-CONTRANS: Semi-supervised medical image segmentation via multi-scale feature fusion and cross teaching of CNN and Transformer, in: IEEE International Symposium on Biomedical Imaging, IEEE. pp. 1–5. doi:10.1109/ISBI56570.2024.10635274.
- Zhou, Z., Siddiquee, M.M.R., Tajbakhsh, N., Liang, J., 2018. UNet++: A nested U-Net architecture for medical image segmentation. *Deep Learning in Medical Image Analysis and Multimodal Learning for Clinical Decision Support*, 3–11doi:10.1007/978-3-030-00889-5_1.